A&A 417, 625–635 (2004)
DOI: 10.1051/0004-6361:20031772

Astronomy & Astrophysics

W Hya: Molecular inventory by ISO-SWS⋆

K. Justtanont[1], T. de Jong[2,3], A. G. G. M. Tielens[4,5], H. Feuchtgruber[6], and L. B. F. M. Waters[3]

[1] Stockholm Observatory, AlbaNova, Dept. of Astronomy, 106 91 Stockholm, Sweden
[2] SRON-Utrecht, Sorbonnelaan 2, 3584 CA Utrecht, The Netherlands
[3] University of Amsterdam, Kruislaan 403, 1098 SJ Amsterdam, The Netherlands
[4] Kapteyn Institute, PO Box 800, 9700 AV Groningen, The Netherlands
[5] SRON-Groningen, PO Box 800, 9700 AV Groningen, The Netherlands
[6] Max-Planck Institut fuer extraterrestrische Physik, Giessenbachstrasse, 85740 Garching, Germany

Received 28 February 2003 / Accepted 16 December 2003

Abstract. Infrared spectroscopy is a powerful tool to probe the inventory of solid state and molecular species in circumstellar ejecta. Here we analyse the infrared spectrum of the Asymptotic Giant Branch star W Hya, obtained by the Short and Long Wavelength Spectrometers on board of the Infrared Satellite Observatory. These spectra show evidence for the presence of amorphous silicates, aluminum oxide, and magnesium-iron oxide grains. We have modelled the spectral energy distribution using laboratory-measured optical properties of these compounds and derive a total dust mass-loss rate of 3×10^{-10} $M_{\odot}$ yr^{-1}. We find no satisfactory fit to the 13 μm dust emission feature and the identification of its carrier is still an open issue. We have also modelled the molecular absorption bands due to H_2O, OH, CO, CO_2, SiO, and SO_2 and estimated the excitation temperatures for different bands which range from 300 to 3000 K. It is clear that different molecules giving rise to these absorption bands originate from different gas layers. We present and analyse high-resolution Fabry-Perot spectra of the three CO_2 bands in the 15 μm region. In these data, the bands are resolved into individual Q-lines in emission, which allows the direct determination of the excitation temperature and column density of the emitting gas. This reveals the presence of a warm ($\simeq$450 K) extended layer of CO_2, somewhere between the photosphere and the dust formation zone. The gas in this layer is cooler than the 1000 K CO_2 gas responsible for the low-resolution absorption bands at 4.25 and 15 μm. The rotational and vibrational excitation temperatures derived from the individual Q-branch lines of CO_2 are different (~450 K and 150 K, respectively) so that the CO_2 level population is not in LTE.

Key words. stars: circumstellar matter – stars: evolution – stars: individual: W Hya – stars: late-type – stars: mass-loss – infrared: stars

1. Introduction

One of the characteristics of Asymptotic Giant Branch (AGB) stars is their mass-loss. As a star evolves up the AGB, its mass-loss rate increases. Just before it evolves off to become a planetary nebula, it sheds most of its mass in a short time, i.e., superwind. Signatures of mass-loss can be studied in the infrared by tracing the dust (e.g., Bedijn 1987; Justtanont & Tielens 1992), and in the sub-millimetre by using molecular rotational lines such as CO (e.g., Knapp & Morris 1985; Groenewegen 1994; Skinner et al. 1999).

An example of an early AGB star is W Hya. It has a relatively low mass-loss rate as deduced from the weak CO millimeter observations (Wannier & Sahai 1986; Bujarrabal et al. 1989; Cernicharo et al. 1997). It is classified as a semiregular variable (SRa) from its light curve. The visual magnitude ranges from 6 to 10 over a period of 382 days (Lebzelter et al. 2000). It exhibits SiO (e.g., Schwartz et al. 1982; Clark et al. 1985), H_2O (e.g., Spencer et al. 1979; Lane et al. 1987) and OH main line masers (e.g., Szymczak et al. 1998; Chapman et al. 1994). It has a weak silicate dust emission at 10 μm along with a smaller emission feature at 13 μm. The carrier of the latter is still being debated. W Hya is one of the first AGB stars for which H_2O rotational emission was reported after the launch of the Infrared Space Observatory (ISO, Kessler et al. 1996). Neufeld et al. (1996) and Barlow et al. (1996) reported that these lines were detected in Short and Long Wavelength Spectrometers (SWS and LWS), respectively. Both authors presented models accounting for the emission. Recently, Zubko & Zuckerman (2000) also reported a model predicting H_2O line fluxes observed by ISO. Also, W Hya has been detected in the

Send offprint requests to: K. Justtanont, e-mail: kay@astro.su.se

⋆ Based on observations with ISO, an ESA project with instruments funded by ESA Member States (especially the PI countries: France, Germany, The Netherlands and the UK) with the participation of ISAS and NASA.

ortho ground state line by SWAS at 557GHz (Harwit & Bergin 2002) In our paper, we mainly discuss the SWS spectra taken during the ISO mission. We also present the SWS Fabry-Perot spectrum of W Hya centered on CO_2 bands. These bands were reported by Ryde (1999) and Justtanont et al. (1998).

2. Observations

Spectroscopic observations of W Hya were taken aboard ISO using both the SWS (de Graauw et al. 1996) and LWS (Clegg et al. 1996). The SWS data were taken using the standard AOT1 (full scan from 2.38–45.2 μm) speed 3, giving an average resolution of 510. We also obtained the spectrum using the full grating resolution of 2000 between 12–16 μm (AOT6) in order to study the CO_2 bands. The data were reduced using the data reduction package provided by the SWS calibration team based at SRON-Groningen. We were able to observe the three CO_2 bands using the SWS Fabry-Perot (FP) centering on the three Q-branches in order to resolve individual transitions. Care was taken to deglitch the spectrum due to cosmic ray hits on the detectors at the time of observation. As the data were taken in small wavelength intervals, each subband spectrum had to be stitched together. The final spectra were rebinned to a resolution of 4×10^4, with an oversampling of 6. Also the flux level for each wavelength band has been normalised to the AOT6 flux.

The LWS data were taken from the archive (PI: Barlow). The reduction was done using the ISAP data reduction package provided by IPAC.

3. Dust and gas mass-loss rates

In this section, we present a model fit to the infrared spectral energy distribution (SED) in order to derive the dust mass-loss rate. This is then used to calculate the rate of gas which is driven by the dust to the observed terminal velocity by momentum transfer between gas and dust. At the same time, the temperature structure of the circumstellar envelope is calculated. The main gas heating is by the dust drag while cooling is done through adiabatic expansion of the gas and radiative cooling via rotational molecular line emission. We also include vibrational cooling by H_2 (Goldreich & Scoville 1976; Justtanont et al. 1994). Hence the dust and gas mass-loss rates are derived in a self-consistent manner. The issue of mass-loss rates is readdressed here as there is a wide range of reported rates from 3×10^{-5} (Neufeld et al. 1996) to 5.2×10^{-8} $M_\odot$ yr^{-1} (Wannier & Sahai 1986); see also Zubko & Elitzur (2000) for a recent reassessment of this controversy.

3.1. The dusty envelope

To derive the dust mass-loss rate, we have fitted the SED of W Hya using ISO SWS and LWS data, together with photometry from ground based observations (Wilson et al. 1972) and the IRAS point source fluxes. We adjusted the flux levels for the LWS spectrum to coincide with the IRAS 60 μm flux which also joins the SWS spectrum very well. There are broad features present in the LWS spectrum which are due to the internal reflection within the instrument at 54 and 110 μm. Here, we calculate the radiative transfer through the dust shell, using a code based on Haisch (1979) which takes into account thermal emission and reemission and multiple scattering. It also allows for a grain size distribution which we assumed to be the same as the interstellar grain sizes (Mathis et al. 1977, hereafter MRN). We also employ multiple grain species.

The input parameters are listed in Table 1. The distance is taken from the Hipparcos catalogue (ESA 1997). From the study by Cami (2002), the emission features between 10–20 μm are a combination of amorphous silicates giving rise to the 10 μm emission, compact Al_2O_3 which gives a feature at 11 μm, spinel ($MgAl_2O_4$) is responsible for the 13 μm feature (Posch et al. 1999), and the 19 μm emission which is attributed to $Mg_{0.1}Fe_{0.9}O$. In our attempt to fit these dust features, we used silicate dust properties employed by Justtanont & Tielens (1992). For other compounds, we extracted the optical constants from the University of Jena database and calculate the extinction coefficients using the Mie theory.

The fit to the SED for a three-dust component model is reasonably good for the complete SWS and LWS data coverage (Fig. 1). The fit is very satisfactory for all observed emission features, providing support for the presence of amorphous silicates, Al_2O_3 and MgFeO, except for the 13 μm feature. A model with spinel which produces a fit to the 13 μm emission feature predicts an additional feature at 16 μm, not seen in the observation (Fig. 2). Hence, while spinel provides a good fit to the 13 μm band, this identification is suspect. Further laboratory studies on related materials are required to test this suggestion. Onaka et al. (1989) suggested aluminum oxide as a carrier for the 13 μm dust emission and following that, Kozasa & Sogawa (1998) were able to explain the 13 μm feature using crystalline aluminum oxide core-silicate mantle grains. However, the optical constants used for aluminum oxide were coarse (1 μm spacing, Toon et al. 1976) and the interpolation of them close to the resonance could result in a misleading profile. A possible carrier proposed by Speck (2000) is SiO_2 which has features at 9.5, 13 and 20 μm while Begemann et al. (1997) suggested a silicate-based material. For the moment, the issue of the dust species responsible for the observed 13 μm feature is still unresolved.

At a distance of 115 pc, we derive a total dust mass-loss rate of 3×10^{-10} $M_\odot$ yr^{-1} for the three species of silicates, Al_2O_3 and MgFeO, assuming a constant outflow velocity of 6 km s^{-1} (Bujarrabal et al. 1989). We note here that we assume that the dust and gas velocity is the same as the fitting of the SED allows us to derive $\dot{M}_{\rm d}/v_{\rm dust}$. We will discuss the effect of the dust drift velocity in Sect. 3.2. Our input values are very similar to those used by Zubko & Elitzur (2000) but we derive a dust mass-loss rate which is lower by a factor of ten. We investigated whether this could be due to the difference in the dust properties used. Zubko & Elitzur used the silicate optical constants derived for AGN dust (Laor & Draine 1993), which has its infrared characteristics based upon astronomical silicates (Draine & Lee 1984). We have also analysed the observed spectra using dust parameters for the astronomical silicates and for $Mg_{0.5}Fe_{0.5}SiO_3$ from the University of Jena database. The derived dust mass-loss rates which fit the observed strength of

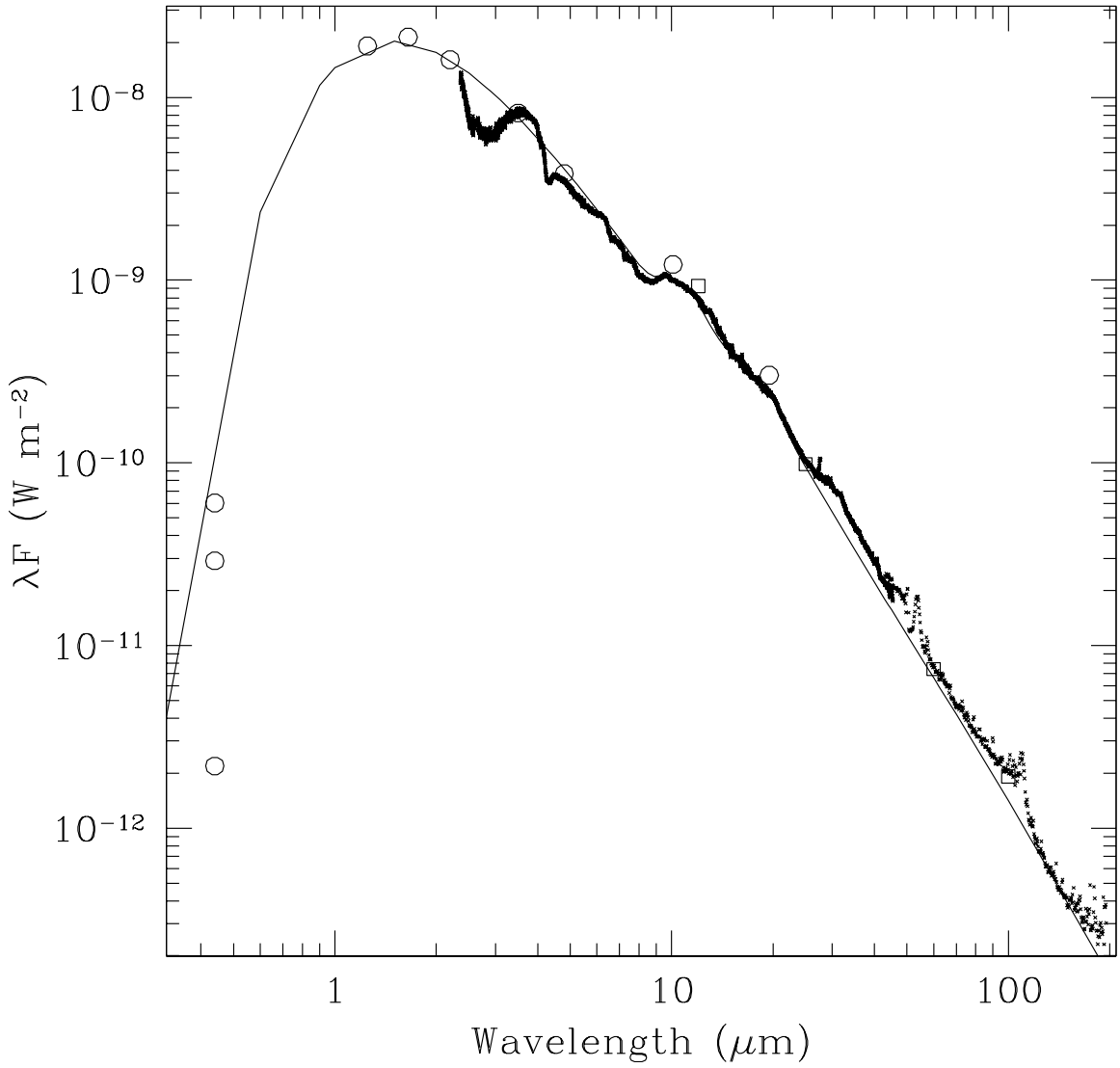

Fig. 1. A fit to the spectral energy distribution of W Hya (solid line) with a three-dust component of amorphous silicates, Al_2O_3 and MgFeO. Open circles are from simbad (V magnitudes) and ground based observations (Wilson et al. 1972) while filled squares are IRAS PSC and crosses are SWS and LWS data. Note that the model does not account for the 13 μm emission feature.

the 10 μm dust feature agree with our value. Hence the difference in the derived dust mass-loss rate is not due to the differences in the optical properties used. Rather, Zubko & Elitzur (2000) did not attempt to fit the observed 10 μm feature in detail, using only ground based-photometry and the ISO-LWS spectrum. We emphasize that the high mass-loss rate of Zubko & Elitzur (2000) gives too strong 10 and 20 μm silicate emission as shown in Fig. 2. We find that extending the calculation to include the dust envelope size observed by IRAS at 60 and 100 μm (Hawkins 1990) does not affect the far-IR flux as the density is far too low in the outer part to affect the SED. For our case, we fitted the silicate 10 μm feature and the other dust species (except for the 13 μm emission feature) which gives a more reliable mass-loss estimate as dust mass-loss rate is proportional to the strength of the 10 μm silicate feature. However, since we did not fit the 13 μm feature, our estimate of the mass-loss rate should be viewed as a lower limit, pending the correct identification of the feature.

If we assume that the elemental abundance of the outflow is that of the Sun, our estimated dust mass-loss rate for each dust component indicates that aluminum condenses out at a higher rate than the silicate, magnesium and iron: the latter three having abundances an order of magnitude higher than that of Al (Anders & Grevesse 1989). The amount of the silicate dust is the same as the aluminum dust while that of MgFeO dust is five times less (Table 1). Thermodynamic consideration of the dust condensation sequence starts with gas phase condensation of Al_2O_3, leading finally to Mg- and Fe-incorporation into silicate grains (Tielens 1990). Alternatively, Al and Si condense out at the same time but as Al has a high affinity for oxygen, aluminum oxide will be formed at a higher rate than silicate (Stencel et al. 1990) thereby giving rise to an 11 μm feature which is as strong as the silicate feature even though the abundance of Al is much lower than that of Si. In either case, the high fraction of Al in dust as compared to Si reflects a freeze-out of the condensation process well before all the

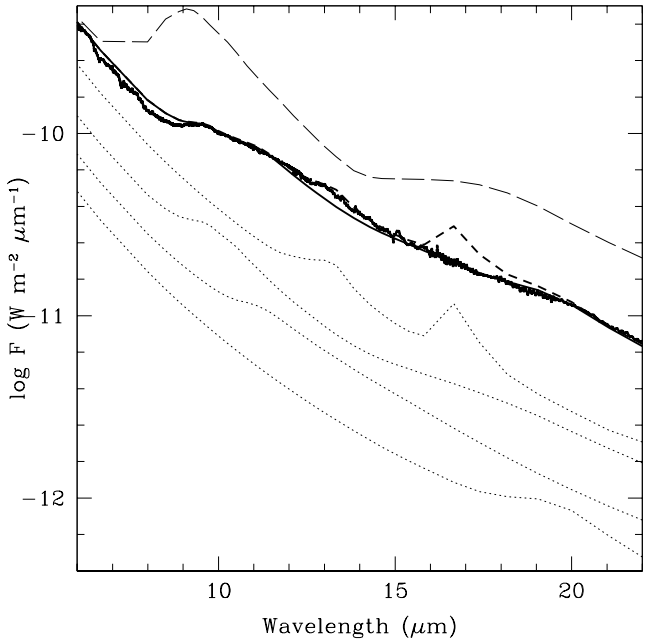

Fig. 2. The plot of a close-up of the dust features. The long dashed line represent a model with Zubko & Elitzur (2000) parameters. The heavy solid line is the three dust model (Fig. 1) while the heavy dashed line is a model which includes spinel. The contribution from individual dust component is shown as dotted lines. From top to bottom: spinel, amorphous silicate, Al_2O_3, and $Mg_{0.1}Fe_{0.9}O$.

silicon has been consumed (e.g., well before magnesium-iron silicates condense out). W Hya is prototypical for a set of O-rich stars which have 10–20 μm spectra which are not dominated by the well-known broad (magnesium/iron) silicate emission features but rather by a set of oxide features (Cami 2002). We surmise that this difference reflects a steep density gradient in the dust condensation layer in these sources as compared to typical Mira variables. The presence of such a steep density gradient is also indicated by the asymmetric light curve of these types of stars.

3.2. The molecular envelope

Using the total dust mass-loss rate obtained by fitting the SED which drives the gas to the terminal velocity, we obtain a dust-to-gas mass ratio of 8.7×10^{-3}, giving a gas mass-loss rate of 3.5×10^{-8} $M_\odot$ yr^{-1} (Model 1) from solving the equation of motion, assuming that the gas and dust are fully momentum coupled.

$$v\frac{\mathrm{d}v}{\mathrm{d}r} = (\Gamma - 1)\frac{GM_*}{r^2} \tag{1}$$

where v is the gas velocity, G is the gravitational constant, M_* is the mass of the star, and Γ is the ratio of the radiation pressure force on dust grains to the gravitational force. Following Justtanont et al. (1994), Γ can be written to include the dust size distribution, $n_\mathrm{d}(a)$, and $Q(a, \lambda)$, the radiation pressure efficiency for a grain size, a, at wavelength λ as

$$\Gamma = \int\int \frac{\sigma_\mathrm{d} Q(a,\lambda) L(\lambda)}{4\pi c G M_*} \frac{n_\mathrm{d}(a)}{\rho} \mathrm{d}\lambda \ \mathrm{d}a \tag{2}$$

Table 1. Input parameters for modelling the dust and gas mass-loss rates in W Hya.

Stellar mass	1 $M_\odot$
Stellar effective temperature	2500 K
Stellar radius	4×10^{13} cm
Outflow velocity	6 km s^{-1}
Distance	115 pc
Dust condensation radius	2×10^{14} cm
Dust mass-loss rates	1.5×10^{-10} $M_\odot$ yr^{-1} – silicates
	1.3×10^{-10} $M_\odot$ yr^{-1} – Al_2O_3
	2.5×10^{-11} $M_\odot$ yr^{-1} – MgFeO
Dust-to-gas mass ratio	8.7×10^{-3}
Gas mass-loss rate	3.5×10^{-8} $M_\odot$ yr^{-1}

where σ_d is the geometric cross section of the dust, $L(\lambda)$ is the luminosity at the wavelength λ, ρ is the gas density (see Justtanont et al. 1994 for full details). We use radiation pressure for purely silicate dust in the calculation of the equation of motion. As a matter of fact, we find that the dust velocity is much greater than that of the gas due to the drift velocity in stars with such a low mass-loss rate.

$$v^2_\mathrm{drift}(a) = \int \frac{Q(a,\lambda)L(\lambda)v}{\dot{M}c}\mathrm{d}a. \tag{3}$$

The drift velocity is calculated for each grain size and then weighted by the size distribution of $a^{-3.5}$. The ratio for the drift velocity for the largest and smallest grains (0.25–0.005 μm) is 8.1. In our calculation, the heating is dominated by the largest grains (heating $\propto v_\mathrm{d}^3$). This results in a high heating rate, therefore the calculated gas kinetic temperature is very high. In the fitting of the SED, we derived an $\dot{M}/v_\mathrm{dust}$ in which we can ignore the drift velocity. However, if we take the drift velocity into account when calculating the dust mass-loss rate and then solve for both the equations of motion and energy balance in a self-consistent way, we derive a mass-loss rate of 1.5×10^{-7} $M_\odot$ yr^{-1} (Model 2) and the calculated CO line fluxes are higher than those observed for the low J transitions (see Table 2). From running a number of models with various different densities and temperatures, we find that the line flux ratio of the CO 2-1/1-0 is a sensitive measure of the assumed mass-loss rate while the temperature plays a minor role. For the observed ratio of 14.7, an upper limit for the mass-loss rate is 8×10^{-8} $M_\odot$ yr^{-1} (Model 3, with the temperature derived from solving the energy balance equation). This model gives the best description of the observed line fluxes from low to higher transitions. As a test, we calculated CO line fluxes using this mass-loss rate and a simple temperature law $T \propto (r/r_i)^{-\alpha}$ where α ranges from 0.5 to 0.8. The resulting line fluxes are insensitive to the change of temperature at this low mass-loss rate ($\leq$10%). This mass-loss rate is within a factor of two of our detailed calculation and puts a stringent upper limit on the mass-loss rate for W Hya. We also calculated the expected CO line fluxes using parameters from Zubko & Elitzur (2000), including their temperature structure. The calculated line fluxes are higher than those by Barlow et al. (1996), reflecting the higher mass-loss rate.

We calculate the peak main beam antenna temperatures for Model 1 to be 0.1 K for CO $J = 1 - 0$ observed with the

Table 2. A comparison of between the observed lines and those from the models using parameters by Barlow et al. (1996) and those derived in this paper. We list the available antenna temperatures ($T_{\rm MB}$), line intensities (I) and line fluxes (F) from various sources.

Transition	Observed	Barlow et al.	Model 1	Model 2	Model 3
$T_{\rm MB}(1-0)$	0.3 K	4.7	0.06	0.4	0.1
$I\,(1-0)$	1.5[a]	55.0	0.8	4.6	1.57
$T_{\rm MB}(2-1)$	2.3 K	20.9	0.7	5.7	1.9
$I\,(2-1)$	22.0[b]	229.6	7.5	51.4	19.3
$F(16-15)$	3.3E-20[c]	8.0E-20	1.6E-20	5.9E-20	2.9E-20
$F(17-16)$	2.3E-20[c]	8.6E-20	1.7E-20	6.2E-20	3.1E-20

[a] CO line intensity (K km s^{-1}) from Bujarrabal et al. (1989).
[b] CO line intensity (K km s^{-1}) Cernicharo et al. (1997).
[c] ISO: Barlow et al. (1996) flux in W cm^{-2}.

IRAM telescope (cf. 0.3 K from Bujarrabal et al. 1989) and 0.7 K for $J = 2 - 1$ observed with a clear double-peaked profile (cf. a flat-top profile with a peak temperature of 2.3 K from Cernicharo et al. 1997), with a canonical value of the CO abundance of 3×10^{-4}. Our calculated gas kinetic temperature, obtained from solving the energy balance, in the outer part of the shell is very high due to the large drift velocity, hence the populations of low-lying levels are excited to higher levels. This, coupled with a low density, results in very low antenna temperatures for $J = 1 - 0$ and $2 - 1$ lines. In order to reconcile these with the observations, we need to increase the mass-loss rate to 8×10^{-8} $M_\odot$ yr^{-1} (Model 3). We also calculated expected line fluxes using input parameters from Barlow et al. (1996) and their temperature, and compared them to the IRAM results plus $J = 16 - 15$ and $J = 17 - 16$ in their ISO-LWS spectrum. The results of these calculations are summarized in Table 2. Our model predicts line fluxes which are lower than the observed values, which is due to the low derived mass-loss rate for lower transitions while Barlow et al.'s parameters predict too high line fluxes by a factor of ten. However, we find that the high rotational lines are insensitive to the input mass-loss rate. The fact that there is a combination of different types of dust, not just silicates, may lead to different radiation pressure. A change in this parameter will affect the drift velocity and hence the heating rate and the gas kinetic temperature. Another factor which affects the CO line fluxes is the adopted turbulent velocity (Kemper et al. 2003). We assume a constant value of 1 km s^{-1} in our calculation but in reality this could vary within the circumstellar envelope. An important issue which we touched upon in the previous section is the dust drift velocity. We calculated the drift velocity of ∼15 km s^{-1} for the averaged radiation pressure for the grains ($\langle Q(a,\lambda)\rangle = 0.0057$). However, the largest grains with a high drift velocity may no longer be momentum-coupled to the gas ($v_{\rm drift} \sim 100$ km s^{-1}!). Hence these grains will not partake in the heating of the gas, and hence the temperature structure of the envelope should be steeper. Further progress in this area has to await a more detailed radiative transfer calculation that includes a realistic model for the heating and cooling.

Our value of the gas mass-loss rate agrees within a factor of two to three with those from Wannier & Sahai (1986) and Olofsson et al. (2002) after scaling for the distance and velocity assumed here. However, our value falls short by an order of magnitude compared with that from Barlow et al. (1996) who calculated radiative transfer for H_2O lines in the LWS wavelength range and from Neufeld et al. (1996) who modelled H_2O lines from the SWS. The gas mass-loss rate derived recently by modelling H_2O emission lines of W Hya by Zubko & Elitzur (2000) is slightly higher than that from Barlow et al. (1996). In an attempt to reconcile these differences, we can say that our assumed CO abundance of 3×10^{-4} may be too high for this object. But we need to reduce this by a factor of 30 to bring the derived mass-loss rate in line with those from the water lines. However, the column density of the CO seen in absorption in SWS seems to contradict the very low abundance (Table 3). The abundance of water used in these calculations may be too low. By increasing the water abundance and lowering the mass-loss rate in those cases, or by increasing our mass-loss rate and lowering the CO abundance in our case, a convergence in mass-loss rate can be found between these approaches. Also, it is difficult to get the kinematic information from ISO LWS observations of H_2O lines because they are not resolved. Although SWAS and Odin observations of the 557 GHz line should be resolved, currently the signal-to-noise ratio is not good enough to be confident about the line profile. In the future it will be possible to study water lines in more detail using the heterodyne instrument (HIFI) aboard the Herschel Telescope due to be launched in 2007 which has a resolution of 1 km s^{-1} or better. Equally important, the collisional cross sections between ortho- and para-H_2O and ortho- and para-H_2 for high temperature extending to high quantum numbers will be available as part of the study project in conjunction with HIFI. In the case where the lines are subthermally excited, the input collisional rates have a strong influence in the calculation of radiative transfer.

4. Modelling absorption bands

The near-IR spectrum of W Hya shows several absorption bands due to various molecules, such as CO, H_2O. In order to see these bands clearly, we divided the spectrum by our fit to the SED and normalised it at 4 μm. We have modelled these absorption bands assuming thermodynamic equilibrium. The molecular data used are taken from Le Floch (1991) for the CO molecule, Schwenke (1998, private communication) for OH and H_2O molecules and Hitran (Rothman et al. 1998) for others. The absorption line profiles are convolved with a Voigt profile with the appropriate full width at half maximum for direct comparison with the observation (see Helmich 1996). From our SED fit to the spectrum, we can define the stellar continuum satisfactorily up to $\lambda \leq 9$ μm. By fitting the observed continuum-divided spectrum with our models, we can derive an excitation temperature ($T_{\rm x}$) for each molecule, along with the column density, N, assuming a Doppler parameter, $b_{\rm D}$. In this paper, we try fitting the different molecular bands independently and derive the best set of parameters for each band. A more sophisticated approach has been made by Cami (2002) using a chi-square technique.

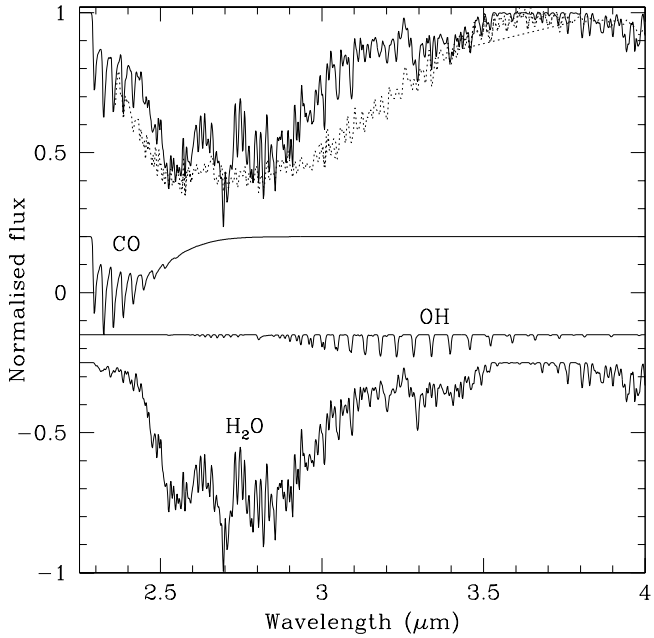

Fig. 3. ISO SWS observation in band 1 (dotted line) compared with the model absorption of CO $\Delta v = 2$, H_2O stretching modes and OH absorption bands (solid line). Each absorption component is also depicted separately.

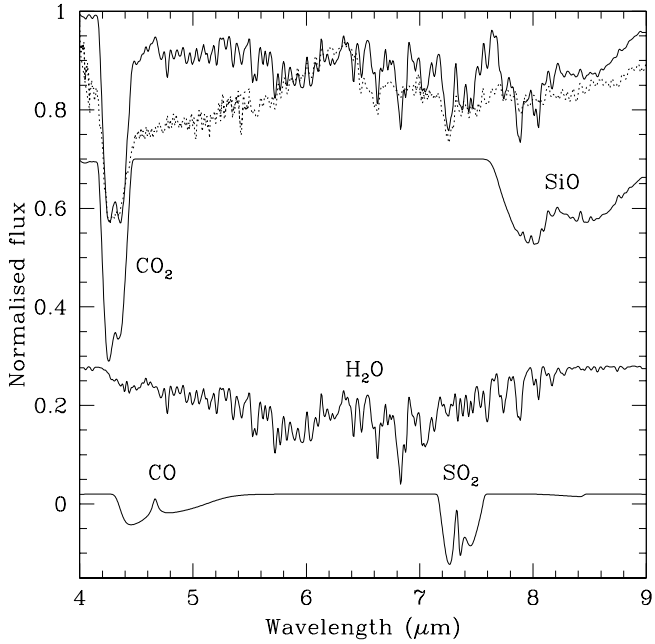

Fig. 4. ISO SWS observation in band 2 (dotted line) compared with the model absorption of CO_2, H_2O bending mode, SO_2 stretching mode and SiO $v = 1 - 0$ band (solid line). Each absorption component is individually shown.

We fitted, in all, six different molecules from 2.3–9 μm. The input parameters are listed in Table 3, while the fits are shown in Figs. 3 and 4. From the temperatures, we can deduce that these molecules originate from different layers in the circumstellar shell. We see bandheads of CO $\Delta v = 2$ from $v = 5$–3 up to $v = 8$–6 which indicates a very hot gas. This is reflected in the input parameter for CO which has a temperature of 3000 K. The column density for the band is high, 10^{21} cm^{-2} also indicating that CO bands originate from a hot, dense region very close to the stellar photosphere. We believe that the gas is possibly excited by shocks since the effective temperature of the star is below the excitation temperature which gives rise to the observed $v = 8$–6 band. This is also consistent with the inferred Doppler width of 9 km s^{-1} used to model the CO absorption band.

We also see the stretching modes of H_2O molecules at 3 μm. We modelled these bands assuming an ortho to para ratio of 3. We are able to reproduce the absorption band relatively well with a gas temperature of 1000 K for the H_2O stretching modes. However, the band is narrower than the observed one, especially in the red wing. The water band overlaps the OH ro-vibrational bands ($\Pi_{3/2}1 - \Pi_{3/2}0$ and $\Pi_{1/2}1 - \Pi_{1/2}0$) which cover from 2.9 to 4 μm. The highly excited lines of OH also indicate that they come from a warm region, close to the star where H_2O is probably photodissociated by shocks. We also modelled the CO_2 stretching mode at 4.25 μm. The band seems to come from the same region as the others. The width of the band is consistent with a gas of 1000 K.

The fit to the bending mode of H_2O at 6 μm is, however, not consistent with the observed data. In view of the various ratios of adjacent lines, we estimate that the excitation temperature is only 300 K for a column density of 5×10^{18} cm^{-2}. The observed absorption is much deeper than calculated in the blue wing where the CO fundamental band is present. The 4.6 μm CO R-branch blends with the CO_2 absorption wing while its P-branch blends with H_2O. At the resolution of the observations, individual absorption lines are not resolved. We roughly estimate the excitation temperature of the CO fundamental absorption to be ~2000 K and put an upper limit for the column density of 10^{19} cm^{-2}. From very high resolution studies of CO lines in Mira variables (Hinkle et al. 1982), different bands come from different regions, with the fundamental band coming from a cool region while the overtone bands come from a hotter region, close to or from the pulsating photosphere. We can also fit the SiO band at 8 μm with a warm gas of 1000 K, possibly from the same layer as the H_2O stretching modes. This is consistent with emission coming from gas interior to the dust forming region where SiO is not bound in dust grains. There is evidence for the weak SO_2 absorption band at 7.3 μm. This band was discovered in a few O-rich AGB stars by Yamamura et al. (1999). We also see CO_2 ν_2 absorption band at 15 μm which we will discuss in more detail in the next section.

Although the overall fit to each band is good, there is still some residue which we are not currently able to account for. There is an absorption band just longward of the 4.25 μm CO_2 band. It is likely that the hotter component of water from the stretching modes contributes between 4.5–6 μm. We compared our results to that from Cami (2002; Table 6.2) and found that although our derived excitation temperatures agree within a factor of two, the column densities are very different (up to two magnitudes difference) in the cases of OH and SiO, while others agree reasonably well. This may lie in the fact that we adopt different Doppler broadening for different regions, i.e., the hotter region has a higher thermal broadening than the cooler one, while Cami (2002) assumed a constant velocity of 3 km s^{-1}

Table 3. Parameters for the spectral absorption calculation. For each molecular band, we also indicate the wavelength coverage.

	λ (μm)	T_x (K)	N (cm^{-2})	b_D (km s^{-1})
CO $\Delta v = 2$	2.3–2.6	3000	1×10^{21}	9
H_2O $\nu_1 + \nu_3$	2.3–4.0	1000	5×10^{20}	7
OH	2.7–4.0	1500	7×10^{17}	8
CO_2 ν_3	4.0–4.6	1000	8×10^{17}	7
CO $v = 1$–0	4.2–5.5	2000	5×10^{18}	8
H_2O ν_2	4.0–9.0	300	5×10^{18}	3
SO_2	7.1–7.7	500	2×10^{17}	3
SiO $v = 1$–0	7.2–9.0	1000	1×10^{19}	7
CO_2 ν_2	14.8–15.0	1000	1×10^{17}	7

Table 4. Line fluxes of rotational water lines detected in the ISO-SWS wavelength range.

Wavelength (μm)	Line flux (W cm^{-2})	Transition
32.98	1.9E-18	$6_{61} - 5_{50}$, $6_{60} - 5_{51}$
35.45	5.3E-19	$5_{33} - 4_{04}$, $7_{43} - 6_{34}$
35.92	4.3E-19	$6_{52} - 5_{41}$, $6_{51} - 5_{42}$
39.35	1.6E-18	$5_{50} - 4_{41}$, $5_{51} - 4_{40}$, $6_{42} - 5_{33}$
40.31	4.8E-19	$6_{43} - 5_{32}$
40.71	1.4E-18	$4_{32} - 3_{03}$, $6_{33} - 5_{24}$
43.91	6.6E-19	$5_{41} - 4_{32}$
44.14	6.1E-19	$5_{42} - 4_{31}$
44.68	4.4E-19	$8_{36} - 7_{25}$
45.10	6.8E-19	$5_{23} - 4_{14}$

throughout. As it turns out, different combinations of column density and Doppler width can give similar resulting absorption. The depth of the absorption is very sensitive to the adopted Doppler velocity used, more so than the column density.

5. Molecular emission lines

Both Barlow et al. (1996) and Neufeld et al. (1996) reported emission due to H_2O rotational lines from LWS and SWS FP mode observations, respectively. From the full SWS scans, we detected 10 more H_2O rotational lines in the region between 30–45 μm. We estimated the line fluxes by assuming a Gaussian profile and these are reported in Table 4. Some lines are a blend of the ortho- and para-water as the wavelengths of their transitions are too close to be resolved by the SWS scan. Barlow et al. (1996) also noted some CO lines present in their LWS spectrum. Surprisingly, only two CO lines have been detected in LWS ($J = 16 - 15$ and $J = 17 - 16$, see Sect. 3). In this section, we will limit our discussion mainly to new results on CO_2.

5.1. The SWS grating spectrum of CO_2

We detected CO_2 in W Hya between 13-16 μm from the full scan SWS AOT1. We see these CO_2 bands in all of the stars which exhibit the so called 13 μm dust feature in our guaranteed time program (PI. de Jong). From this we proposed that objects with the 13 μm dust have CO_2 associated with it

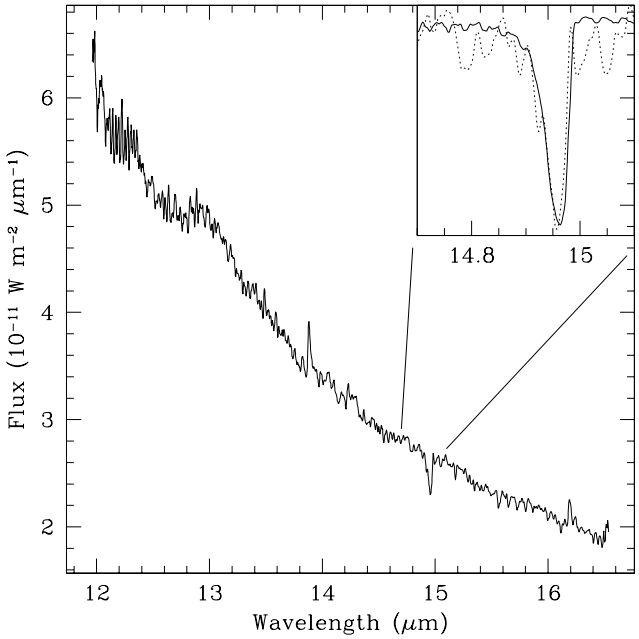

Fig. 5. The full grating resolution spectrum of W Hya, showing the 13 μm dust and CO_2 bands. The insert show the modelled absorption (solid line) compared to the observed spectrum (dotted line).

(see Justtanont et al. 1998, Fig. 1). On this basis, we obtained further observing time to scan objects with this dust feature at the highest grating resolution (AOT6). All the objects observed in the supplementary program confirm our idea, i.e., all stars with the 13 μm dust show CO_2 bands. However, the reverse is not always the case, e.g., one of the stars in our program, *o* Ceti, has no 13 μm dust but shows CO_2 emission and IRC+10011 also shows CO_2 while the 10 μm silicate is self-absorbed (Markwick & Millar 2000). Cami et al. (2000) show a detailed calculation of CO_2 emission bands in EP Aqr, one of the stars in our program. If the association between the 13 μm dust feature and CO_2 gas is real then CO_2 is very prevalent because Sloan et al. (1996) argue that up to 50% of O-rich semiregular variables show such a dust feature. The formation of CO_2 is thought to be via CO+OH (Nercessian et al. 1989; Willacy & Millar 1997) where OH is the product of either photodissociation or of shock destruction of H_2O molecules.

In W Hya, the transitions $10^00 - 01^10$ at 13.87 μm and $02^00 - 01^10$ at 16.18 μm are in emission while $01^10 - 00^00$ at 14.97 μm is in absorption. We modelled the absorption band which is shifted from the normal position as seen in emission in other stars. We attribute this shift towards a shorter wavelength to the importance of highly excited bands. To excite these bands (e.g., $02^20 - 01^10$, $03^30 - 02^20$, $04^40 - 03^30$), we need the gas temperature to be ~1000 K (Fig. 5). These bands have their Q-branches at successively shorter wavelengths than the $01^10 - 00^00$ band. By including these bands in our calculation, we are able to match the peak absorption at 14.957 μm as observed. One thing to note from our observations of objects with CO_2 is that only stars with the 14.97 μm absorption show the corresponding 4.25 μm absorption. Those which show the 14.97 μm in emission lack the stretching mode counterpart (for the full sample, see Cami 2002). This probably indicates

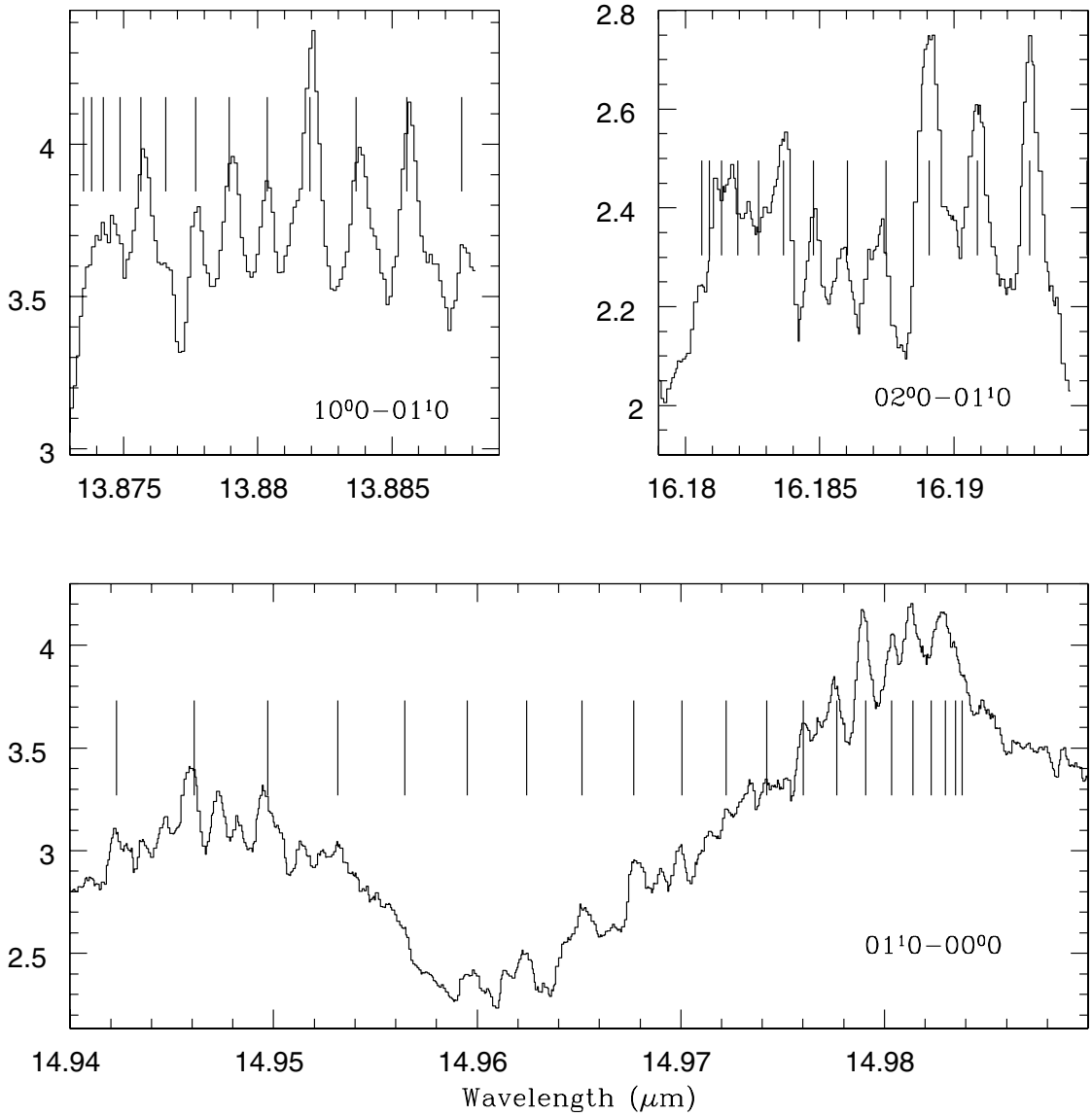

Fig. 6. SWS-FP observations of CO_2 in W Hya with the wavelength corrected for the heliocentric velocity. The top panels show the partly resolved Q-branches of the 13.87 and 16.18 μm bands and the bottom panel shows the 14.97 μm band. Flux units are 10^{-11} W m^{-2} μm^{-1}. Vertical lines indicate positions of Q lines. The first few Q lines are not resolved.

that the radiative pumping by the 4.25 μm band plays a very minor role, if at all, in populating the levels which result in the 13–16 μm emission.

5.2. The Fabry-Perot observation of CO_2 bands

We subsequently obtained high resolution spectra of these CO_2 bands using the SWS-FP which resolved the individual Q branches (Fig. 6). The small dip at 13.877 μm in the band 10^00-01^10 in this figure is an instrumental effect due to the end of the scan of FP wavelength setting. The resolved Q-lines are listed in Table 5 where the wavelength, the energy of the upper level, the measured line flux and the identification are given. The flux errors given represent the estimated uncertainties in the continuum and do not take into account possible calibration errors so that they should be taken as lower limits.

It is quite remarkable though that we can discern emission of the Q-branch lines in the depth of the 14.97 μm band while the absorption blends into a single band. As discussed in Sect. 5.1, this absorption is formed in a hot (1000 K) gas layer in the outer photosphere and lines may be smeared out by turbulence (b_D = 7 km s^{-1}, see Table 3) and/or optical depth effects. The first of the individual Q-line to be resolved in emission is Q10. The close spacing between Q2–Q8 means that even at this resolution we cannot separate them from each other. We conclude that the emission lines are produced in a gas layer which is more extended and lying farther out in the circumstellar shell than the hot layer which is responsible for the absorption band at 14.95–14.98 μm, in line with earlier suggestions by Justtanont et al. (1998) and Cami et al. (2000).

We have Fabry-Perot observations of individual Q-branch lines for three bands of CO_2 (see Fig. 6). In the fundamental

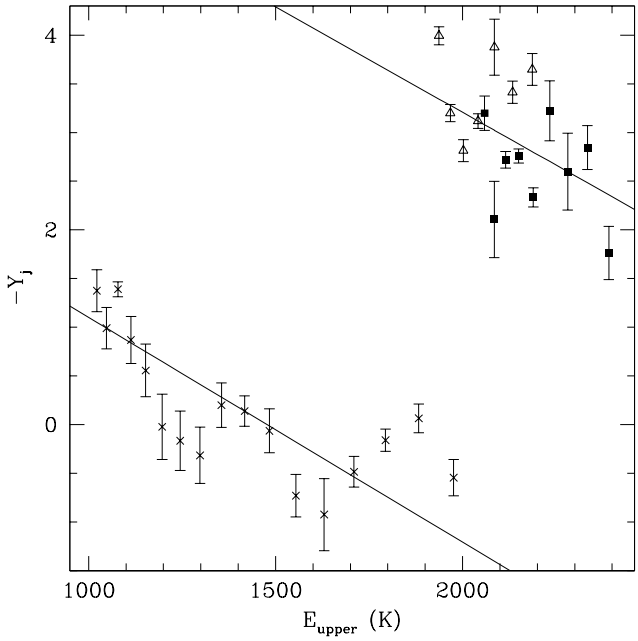

Fig. 7. The rotation diagram of CO_2. Crosses are from the 01^10-00^00, triangles represent the 02^00-01^10 and squares represent 10^00-01^10. The solid lines are the best fit for these bands.

band we detected lines up to Q42 and in the other bands up to Q24. We can use the observed flux of the individual line in each band to construct a rotation diagram from which we can derive a rotational excitation temperature $T_{\rm rot}$ characterizing the population distribution within the upper vibrational level of each band, using the relation

$$E_j/kT_{\rm rot} = \ln(N_v/\Phi(T_{\rm rot})d^2) - \ln(4\pi F_{ji}/A_{ji}h\nu_{ji}g_j) \equiv \ln(N_v/\Phi(T_{\rm rot})d^2) - Y_j \quad (4)$$

where E_j and g_j are the energy and statistical weight of the upper state, F_{ji} and ν_{ji} are the line flux and frequency of the transition, A_{ji} is the spontaneous transition probability, N_v is the total number of molecules in the upper vibrational level v, $\Phi(T_{\rm rot})$ is the partition function, and d is the distance to W Hya. Figure 7 shows the rotation diagram of all the resolved Q-lines. There is considerable scatter in the data points due to uncertainties in the calibration (e.g., joining of different pieces of the spectrum within each band) and in the continuum. The offset between the data points in the 01^10 level and in the 02^00 and 10^00 levels is due to differences in the number of molecules in these levels.

In Table 6, we collect a number of quantities derived from the fits in Fig. 7. The derived rotation temperatures are 435 K for the 01^10 level and 460 K for the other two levels combined. The partition functions for each vibrational level are computed assuming that the levels are populated in thermal equilibrium at the rotational temperature. The quantities Y_0 are the intercepts of the fits in Fig. 7 at $E_j = 0$. Putting $E_j = 0$ and $Y_j = Y_0$ in Eq. (3) we derive values of N_v, the total number of molecules in each vibrational level, listed in Col. 5 of Table 6. These numbers are a lower limit as we assumed that the lines are optically thin.

Table 5. A list of the CO_2 emission lines detected from the FP observations.

Wavelength (μm)	$E_{\rm upper}$ (K)	Line flux (10^{-19} W cm^{-2})	Transition
13.87564	2059.0606	2.6 ± 0.5	10^00-01^10 Q10
13.87658	2084.8831	1.0 ± 0.5	10^00-01^10 Q12
13.87768	2115.1954	2.2 ± 0.2	10^00-01^10 Q14
13.87894	2149.9974	2.7 ± 0.2	10^00-01^10 Q16
13.88036	2189.2882	1.9 ± 0.2	10^00-01^10 Q18
13.88194	2233.0677	5.3 ± 1.9	10^00-01^10 Q20
13.88367	2281.3351	3.1 ± 1.5	10^00-01^10 Q22
13.88556	2334.0896	4.3 ± 1.1	10^00-01^10 Q24
13.88760	2391.3305	1.6 ± 0.5	10^00-01^10 Q26
14.94229	1976.2415	1.6 ± 0.3	01^10-00^00 Q42
14.94609	1882.9064	2.8 ± 0.5	01^10-00^00 Q40
14.94972	1794.0594	2.1 ± 0.3	01^10-00^00 Q38
14.95317	1709.7018	1.5 ± 0.3	01^10-00^00 Q36
14.95643	1629.8354	0.9 ± 0.4	01^10-00^00 Q34
14.95952	1554.4611	1.0 ± 0.3	01^10-00^00 Q32
14.96243	1483.5803	1.9 ± 0.5	01^10-00^00 Q30
14.96515	1417.1943	2.1 ± 0.4	01^10-00^00 Q28
14.96769	1355.3043	2.1 ± 0.5	01^10-00^00 Q26
14.97005	1297.9109	1.2 ± 0.4	01^10-00^00 Q24
14.97223	1245.0155	1.2 ± 0.4	01^10-00^00 Q22
14.97422	1196.6187	1.3 ± 0.5	01^10-00^00 Q20
14.97603	1152.7216	2.1 ± 0.7	01^10-00^00 Q18
14.97765	1113.3246	2.6 ± 0.7	01^10-00^00 Q16
14.97909	1078.4285	3.8 ± 0.3	01^10-00^00 Q14
14.98034	1048.0339	2.2 ± 0.5	01^10-00^00 Q12
14.98141	1022.1414	2.7 ± 0.7	01^10-00^00 Q10
16.18366	1937.0742	4.2 ± 0.2	02^00-01^10 Q12
16.18476	1967.4081	2.2 ± 0.2	02^00-01^10 Q14
16.18603	2002.2345	1.7 ± 0.2	02^00-01^10 Q16
16.18747	2041.5522	2.5 ± 0.2	02^00-01^10 Q18
16.18908	2085.3610	6.0 ± 2.0	02^00-01^10 Q20
16.19087	2133.6598	4.1 ± 0.5	02^00-01^10 Q22
16.19283	2186.4477	5.6 ± 0.1	02^00-01^10 Q24

Table 6. Quantities derived from the rotation diagram.

Level	$T_{\rm rot}$ (K)	$\Phi(T_{\rm rot})$	Y_0	N_v
10^00	460	4.73	−7.57	3.0×10^{38}
02^00	460	6.56	−7.50	4.2×10^{38}
01^10	435	47.2	−3.20	2.4×10^{41}

From these, we then find the vibrational excitation temperatures $T_{\rm vib}$ (10^00-01^10) = 150 K and $T_{\rm vib}$ (02^00-01^10) = 170 K, using the relation $T_{\rm vib} = 1.44\ E_{ij}/\ln(N_j/N_i)$ with $E(10^00-01^10) = 720$ cm^{-1} and $E(02^00-01^10) = 617$ cm^{-1} and taking into account that the number of rotational levels in level 01^10 is twice as large (J = even and odd) as in levels 10^00 and 02^00 (J = even only). Assuming that the relative number of molecules in the ground vibrational state 00^00 and the first excited vibrational state 01^10 is also characterized by $T_{\rm vib} \sim 160$ K we find a total number of CO_2 molecules of 5×10^{43}.

Clearly the temperature characterizing the distribution of rotational levels in the vibrational states of CO_2 (~450 K) is different from the temperature characterizing the distribution of molecules over the vibrational states (~160 K) so that the CO_2 molecules are close to, but not in thermal equilibrium. This non-LTE behaviour can be understood on the basis of the symmetry of the CO_2 molecule which does not allow pure rotational radiative transitions and the magnitudes of the cross sections for (de-)excitation of CO_2 by collisions with H_2, which are about three orders of magnitude larger for pure rotational transitions than for ro-vibrational transitions (Banks & Clary 1987). It can be shown by more detailed non-LTE multi-level line transfer calculations (de Jong, in preparation) that at a few stellar radii from the star and at H_2 densities above $\sim 10^8$ cm^{-3} the rotational levels are more strongly coupled to the gas kinetic temperature (~400 K) while the population of the vibrational levels is dominated by radiation trapping in the ro-vibrational lines (the ones that we observe) resulting in a vibrational temperature somewhat below the kinetic temperature.

We suggest that CO_2 absorption and emission originate in two different regions of an extended dynamical atmosphere: one close to the star in the outer photosphere where the temperature is 1000 K, giving rise to the absorption seen at 4.25 and 14.95 μm, and the other farther out at few stellar radii, where the density is still high enough to thermally distribute the pure rotational levels at ~450 K. Assuming that the cooler CO_2 layer is located at ~3 stellar radii we find, from the total number of molecules observed, a column density $N(CO_2) \sim 10^{15}$, two orders of magnitude smaller than that derived for the hot CO_2 gas (see Table 3) and also several orders of magnitude smaller than found for the warm gas in the star EP Aqr by Cami et al. (2000)

As proposed earlier by Tsuji et al. (1997), Yamamura et al. (1999), and Cami et al. (2000), we believe that the emission line gas detected here is part of the warm gas layer located between the stellar photosphere and the dust condensation zone. This gas is probably related to the blown-up atmosphere observed by Reid & Menten (1990) and found by Höfner et al. (1998) in their calculations of the dynamical atmospheres of pulsating stars. How CO_2 molecules are formed in this gas is unclear but they may well be a left-over from the preceding photosphere phase. According to Höfner et al. (1998), this gas is expected to have turbulent velocities of order 1 km s^{-1}. Eventually a little further out (at ~5 stellar radii) the dust is formed which then accelerates the flow to 5–10 km s^{-1}. The CO_2 is probably quickly photodissociated in the expanding envelope. We note here that the line widths of the emission are much narrower than those of the absorption, suggesting that the emission comes from a cooler (since we do not see higher overtone bands in emission), much less turbulent layer than that which produces the absorption. Whether the hot and cool layers of CO_2 are manifestations of the same gas needs to be investigated further in a detailed model for CO_2 excitation.

6. Summary

By fitting the SED of W Hya from the near- to far-IR, we derive a dust mass-loss rate of 3×10^{-10} $M_\odot$ yr^{-1} using a combination of three different dust species of amorphous silicate, Al_2O_3 and MgFeO. We also tried adding a fourth component of spinel to account for the 13 μm dust feature but in order to fit it, we also expect to see another strong peak at 16 μm which is not present in the observed spectrum. From this, we conclude that spinel cannot be the carrier of the 13 μm dust emission feature. Hence, the debate on the carrier of the 13 μm feature is still open. With the estimated value of the our dust mass-loss rate, we get a gas mass-loss rate range of (3.5–8)$\times 10^{-8}$ $M_\odot$ yr^{-1} from simple consideration of momentum dust driven wind. Our derived mass-loss rate agrees well with those previously derived to explain the CO emission, taking into account the differences in the adopted distance and velocity. However, the discrepancy still exists between these mass-loss rates and those derived from the H_2O emission, the latter being consistently higher. The difference in derived mass-loss rates from CO and H_2O may simply be due to the abundances assumed for each species.

We obtained the full scan SWS spectrum of W Hya in which we modelled the absorption bands due to various molecules. The derived excitation temperatures of different bands suggest that they originate from different layers of gas, from 300 K to 3000 K. However, some molecules exist over a wide range of temperatures and cannot really be stratified within a particular zone, particularly those which show multiple absorption bands. The exception may be OH which is a product of water molecules which are dissociated by shocks in the inner part of the envelope.

We also observed CO_2 bands in emission using SWS FP and were able to resolve the three strongest Q branches in the mid-IR. The resulting rotation diagram yields an excitation temperature of ~450 K while the CO_2 absorption at 14.97 μm requires a gas of 1000 K to explain the shift of the peak absorption bluewards. The stretching mode at 4.25 μm also requires a layer of hot gas to explain its width. We find from simple calculation based on the rotation diagram that the vibrationally excited levels may not be in LTE. Whether the CO_2 absorption and emission lines can indeed be explained by temperature stratification in an extended dynamical atmosphere needs to be investigated in a more detailed radiation transfer model.

Acknowledgements. We are grateful to our referee, Dr. J Alcolea for constructive comments which improves the discussion in our paper. This research has made use of the SIMBAD database, operated at CDS Strasbourg, France.

References

Anders, E., & Grevesse, N. 1989, Geochim. Cosmochim. Acta, 53, 197
Banks, A. J., & Clary, D. C. 1987, J. Chem. Phys., 86, 802
Barlow, M. J., Nguyen-Q-Rieu, Truong-Bach, et al. 1996, A&A, 315, L241
Bedijn, P. J. 1987, A&A, 186, 136
Begemann, B., Dorschner, J., Henning, T., et al. 1997, A&A, 476, 199
Bujarrabal, V., Gómez-González, J., & Planesas, P. 1989, A&A, 219, 256
Cami, J., Ph.D. Thesis, University of Leiden

Cami, J., Yamamura, I., de Jong, T., et al. 2000, A&A, 360, 562
Cernicharo, J., Alcolea, J., Baudry, A., & Gonz'alez-Alfonso, E. 1997, A&A, 319, 607
Chapman, J. M., Sivagnanam, P., Cohen, R. J., & Le Squeren, A. M. 1994, MNRAS, 268, 475
Clark, F. O., Troland, T. H., & Miller, J. S. 1985, ApJ, 289, 756
Clegg, P., Ade, P. A. R., Armand, C., et al. 1996, A&A, 315, L38
de Graauw, T., Haser, L. N., Beintema, D. A., et al. 1996, A&A, 315, L49
Draine, B. T., & Lee, H. M. 1984, ApJ, 285, 89
ESA 1997, the Hipparcos and Tycho Catalogues, ESA SP-1200
Gilman, R. C. 1972, ApJ, 178, 423
Goldreich, P., & Scoville, N. 1976, ApJ, 205, 144
Groenewegen, M. A. T. 1994, A&A, 290, 531
Haisch, B. M. 1979, A&A, 72, 161
Harwit, M., & Bergin, E. A. 2002, ApJ, 565, L105
Hawkins, G. W. 2000, A&A, 229, L5
Helmich, F. P. 1996, Ph.D. Thesis (Leiden)
Hinkle, K. H., Hall, D. N. B., & Ridgway, S. T. 1982, ApJ, 252, 697
Höfner, S., Jørgensen, U. G., Loidl, R., & Aringer, B. 1998, A&A, 340, 497
Justtanont, K., Feuchtgruber, H., de Jong, T., et al. 1998, A&A, 330, L17
Justtanont, K., Skinner, C. J., & Tielens, A. G. G. M. 1994, ApJ, 435, 852
Justtanont, K., & Tielens, A. G. G. M. 1992, ApJ, 389, 400
Kemper, F., et al. 2003, A&A, submitted
Kessler, M. F., Steinz, J. A., Anderegg, M. E., et al. 1996, A&A, 315, L27
Knapp, G. R., & Morris, M. 1985, ApJ, 292, 640
Kozasa, T., & Sogawa, H. 1998, Ap&SS, 255, 437
Lane, A. P., Johnston, K. J., Bowers, P. F., Spencer, J. H., & Diamond, P. J. 1987, ApJ, 323, 756
Laor, A., & Draine, B. T. 1993, ApJ, 402, 441
Le Floch, A. 1991, Mol. Phys., 72, 133
Lebzelter, T., Kiss, L. L., & Hinkle, K. H. 2000, A&A, 361, 167
Markwick, A. J., & Millar, T. J. 2000, A&A, 359, 1162
Mathis, J. S., Rumple, W., & Norsieck, K. H. 1977, ApJ, 217, 425
Nercessian, E., Guilloteau, S., Omont, A., & Benayoun, J. J. 1989, A&A, 210, 225
Neufeld, D. A., Chen, W., Melnick, G. J., et al. 1996, A&A, 315, L237
Olofsson, H., Gonzales-Delgado, D., Kerschbaum, F., & Schöier, F. L. 2002, A&A, 391, 1053
Onaka, T., de Jong, T., & Willem, F. J. 1989, A&A, 218, 169
Posch, T., Kerschbaum, F., Mutschke, H., et al. 1999, A&A, 352, 609
Reid, M. J., & Menten, K. M. 1990, ApJ, 360, L51
Rothman, L. S., Rinsland, C. P., Goldman, S. T., et al. 1998, J. Quant. Spectrosc. Radiat. Transfer, 60, 665
Ryde, N., Eriksson, K., & Gustafsson, B. 1999, A&A, 341, 579
Schwartz, P. R., Zuckerman, B., & Bologna, J. M. 1982, ApJ, 256, L55
Skinner, C. J., Justtanont, K., Tielens, A. G. G. M., Betz, A. L., & Boreiko, R. T. 1999, MNRAS, 302, 296
Sloan, G. C., LeVan, P. D., & Little-Merenin, I. R. 1996, ApJ, 463, 310
Speck, A. K., Barlow, M. J., Sylvester, R. J., & Hofmeister, A. M. 2000, A&AS, 146, 437
Spencer, J. H., Johnston, K. J., Moran, J. M., et al. 1979, ApJ, 230, 449
Stencel, R. E., Nuth, J. A., Little-Marenin, I. R., & Little, S. J. 1990, ApJ, 350, L45
Szymczak, M., Cohen, R. J., & Richards, A. M. S. 1998, MNRAS, 297, 1151
Tielens, A. G. G. M. 1990, in From Miras to Planetary Nebulae: Which path for stellar evolution?, ed. M. O., Mennessier, & A., Omomt (France: Éditions Frontières), 186
Toon, O. B., Pollack, J. B., & Khare, B. N. 1976, J. Geophys. Res., 81, 5733
Tsuji, T., Ohnaka, K., Yamamura, I. 1997, A&A, 320, L1
Wannier, P. G., & Sahai, R. 1986, ApJ, 311, 335
Willacy, K., & Millar, T. J. 1997, A&A, 324, 237
Wilson, W. J., Schwartz, P. R., Neugebauer, G., Harvey, P. M., & Becklin, E. E. 1972, ApJ, 177, 523
Yamamura, I., de Jong, T., Onaka, T., Cami, J., & Waters, L. B. F. M. 1999, A&A, 341, L9
Zubko, V., & Elitzur, M. 2000, ApJ, 554, L137